ACS APPLIED MATERIALS & INTERFACES

Research Article

www.acsami.org

Three-Dimensional Morphological and Chemical Evolution of Nanoporous Stainless Steel by Liquid Metal Dealloying

Chonghang Zhao,[†] Takeshi Wada,[‡] Vincent De Andrade,[§] Garth J. Williams,[∥] Jeff Gelb,[⊥] Li Li,[∥] Juergen Thieme,[∥] Hidemi Kato,[‡] and Yu-chen Karen Chen-Wiegart*[,†,∥]

[†]Department of Materials Science and Chemical Engineering, Stony Brook University, Stony Brook, New York 11794, United States

[‡]Institute for Materials Research, Tohoku University, Katahira, Sendai 980-8577, Japan

[§]Advanced Photon Source, Argonne National Laboratory, Argonne, Illinois 60439, United States

[∥]National Synchrotron Light Source II, Brookhaven National Laboratory, Upton, New York 11973, United States

[⊥]ZEISS Group, Carl Zeiss X-ray Microscopy, Inc., Pleasanton, California 94588, United States

Supporting Information

ABSTRACT: Nanoporous materials, especially those fabricated by liquid metal dealloying processes, possess great potential in a wide range of applications due to their high surface area, bicontinuous structure with both open pores for transport and solid phase for conductivity or support, and low material cost. Here, we used X-ray nanotomography and X-ray fluorescence microscopy to reveal the three-dimensional (3D) morphology and elemental distribution within materials. Focusing on nanoporous stainless steel, we evaluated the 3D morphology of the dealloying front and established a quantitative processing−structure−property relationship at a later stage of dealloying. The morphological differences of samples created by liquid metal dealloying and aqueous dealloying methods were also discussed. We concluded that it is particularly important to consider the dealloying, coarsening, and densification mechanisms in influencing the performance-determining, critical 3D parameters, such as tortuosity, pore size, porosity, curvature, and interfacial shape.

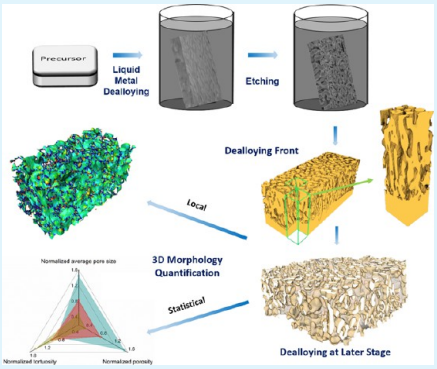

KEYWORDS: *nanoporous, stainless steel, tomography, dealloying, X-ray CT, XRF*

1. INTRODUCTION

Nano-/mesoporous metals fabricated by different methods,[1] including chemical dealloying,[2] electrochemical dealloying,[3,4] template methods,[5,6] and additive manufacturing,[7] have received great attentions. Although additive manufacturing and template methods offer a range of processes to fabricate different metal architectures for medical[8] and optical industries,[9] dealloying remains as an attractive method to fabricate bicontinuous open porous structures. The self-organizing process in dealloying is particularly attractive for fabricating fine structures at nano-/mesoscales. The resulting porous metals exhibit a tunable feature size, retention of precursor microstructure,[10] and a bicontinuous structure, which provides not only the open pores for materials transport but also a solid phase for self-support or electron/thermal conduction. Thus, a range of diverse applications as functional materials have been invented on the basis of dealloyed nano-/mesoporous metals and alloys for catalysts,[11−15] fuel cells,[16] radiation damage-resistant materials,[17] nanocomposites,[18] sensors,[19] actuators,[20] and electrodes in energy storage devices, such as batteries[21] and supercapacitors.[22]

Conventionally, dealloying is carried out by leaching in aqueous solutions (acid or base), which yields a range of materials with novel applications. Instead of an acid or base solution, a metal can be used as a dealloying agent to introduce dealloying and phase separation. This concept was studied in a pioneer work by Harrison et al.;[23] however, only until very recently, the method has been further explored as a novel method to fabricate nanoporous materials[24] or nanocomposites.[25] This provides an alternative route to fabricate an even wider range of bicontinuous porous materials, such as nanoporous titanium,[26] steel,[27] and silicon,[21] for a range of applications. Liquid metal dealloying involves introducing a metal to a precursor alloy to cause dealloying, leading to a bicontinuous structure due to the right combination of mix enthalpy. One of the phases can then be removed from the bicontinuous composite, resulting in a nanoporous structure.[28] Nanoporous stainless steel (np-ss) fabricated by this method is particularly promising, with great industrial applications and socioeconomic impact. For instance, for energy conversion devices, the metallic nanoporous structure can potentially provide an alternative to the carbon-based materials that serve as the gas diffusion layer in proton exchange membrane fuel cells,[29,30] to provide a better structural support.[31,32] In addition,

Received: April 1, 2017
Accepted: September 4, 2017
Published: September 4, 2017

DOI: 10.1021/acsami.7b04659
ACS Appl. Mater. Interfaces 2017, 9, 34172−34184

the open-pore and high-surface-area properties can make the materials suitable for use as the substrate in energy storage devices, such as batteries and supercapacitors, as well as catalysts or supports for catalysts.

Despite of the promises offered by these materials, it has been a challenge to obtain comprehensive process−structure−property information for best optimizing their performance for potential applications, such as energy storage and conversion devices. In previous studies, characterization methods, including scanning electron microscopy (SEM) and transmission electron microscopy (TEM), were used to analyze nanoporous stainless steel fabricated by liquid metal dealloying. However, the morphology analysis is mostly limited to imaging the surfaces and cross sections of the materials in two dimensions (2D). Focused ion beam-SEM (FIB-SEM) has been employed in an attempt at revealing the 3D character,[28] but quantification of the structure remains elusive for this new class of materials. In addition to characterizing the final structure in 3D, revealing the morphology of the materials at the early dealloying stage could also lead to a better understanding of the dealloying mechanism. McCue et al. presented an in-depth analysis on the dealloying kinetics of another liquid metal dealloying system, Ti−Ta alloys immersed in molten Cu,[33] utilizing 2D SEM cross sections to study the morphology. Geslin et al.[34] studied the topological variation during liquid metal dealloying as a function of alloy composition with 2D and 3D simulation, with experimental results in 2D presented. However, 3D imaging of the dealloying front[35] has yet to be presented in experiments. On the other hand, a wide range of 3D techniques have been used to characterize nanoporous metals fabricated by dealloying in aqueous solutions; many of the works have been done particularly on nanoporous gold, which is a classic example of dealloying by aqueous solutions. For instance, Fujita et al. and Rosner et al. independently carried out TEM tomography,[36,37] Lilleodden et al. conducted FIB-SEM tomography,[38] and Chen-Wiegart et al. conducted X-ray nanotomography;[39] these 3D imaging techniques were applied to understand the 3D morphology of nanoporous gold, both as-dealloyed and during coarsening. More recently, Krekeler et al. have mapped the elemental distribution in nanoporous gold in 3D using TEM tomography; their results highlight the distribution of residual silver clusters in the nanoporous gold and their homogenization after annealing.[40] Pfeiffer and Volkert et al. used atom probe tomography (APT) to study the local chemistry of nanoporous gold with subnanometer resolution; by filling the pores with electron-beam-induced deposition, they overcame the challenge that the APT is generally difficult to be applied to porous materials.[41] These studies demonstrated that 3D characterization tools can bring insights into both understanding the mechanisms of the 3D morphological evolution and quantifying the final dealloyed structures in 3D.

Here, we aim to address this interest by conducting a systematic analysis of 3D morphological and chemical evolution during liquid metal dealloying process in np-ss, quantifying on critical 3D parameters. To achieve this aim, we first discuss the morphological heterogeneity at the dealloying front, corresponding to an early dealloying stage. Three-dimensional X-ray nanotomography results were compared with the simulation conducted by Geslin et al.,[34] quantifying the ligament-size evolution near the dealloying front. Second, the 3D morphology of np-ss materials at a later dealloying stage was studied to address the process−structure−property relationship for potential applications. We quantify the influence of different dealloying conditions, including dealloying time, dealloying temperature, and precursor composition, on 3D morphological properties, including porosity, average pore size, tortuosity, pore size distribution, curvature, and interfacial shape, using synchrotron X-ray nanotomography. Tortuosity (τ) is an important parameter defined as the effective diffusion length divided by the straight distance, which is a key in determining the transport properties of materials. X-ray fluorescence (XRF) microscopy was also used to show the elemental distributions in the materials after dealloying. We compared the microstructural characteristics of the nanoporous metals fabricated by liquid metal dealloying to those of the structures fabricated by the more conventional aqueous solution dealloying. This liquid metal dealloying process is different from the more conventional dealloying method in terms of the dealloying agent—a metal is used to introduce the phase separation, instead of an acid or base aqueous solution; however, the resulting final structures display many similarities among these two approaches. Nevertheless, the samples made from these two dealloying methods still exhibit some morphological differences, particularly near the dealloying front. The higher temperature used in this process also tends to lead to larger pores and ligaments, lower tortuosity, as well as a porous gradient as quantified in this work. The nanoporous structure can ultimately be optimized to the desired application, by tailoring critical 3D morphological parameters.

2. EXPERIMENTAL SECTION

2.1. Sample Preparation and SEM Characterization. First, pure Fe, Cr, and Ni (99.99%) were prepared into a precursor alloy by arc melting; the Fe−Cr−Ni alloy was cold-rolled to sheets with less than 100 μm thickness. The sheets were cut into rectangular shapes of 10 mm × 20 mm. The final composition of the precursors was $(Fe_{0.8}Cr_{0.2})_{1-x}Ni_x$, where x = 30, 50, and 70% atomic ratio is the first controlled parameter. Under high-purity helium environment, pure Mg in a carbon crucible was heated to either 973 K (700 °C) or 1073 K (800 °C) as our second controlled parameter. The precursor was then immersed into the Mg metallic melt and dealloyed for 1, 5, or 10 min, which is the third controlled parameter. Mg gradually penetrates the precursors and removes Ni from the Fe−Cr phase, causing a dealloying of the original precursor; this phase separation process produces liquid Mg−Ni and solid Fe−Cr, a bicontinuous structure. Removing the precursor from the Mg bath and cooling it to room temperature results in a solid composite of Mg−Ni and Fe−Cr. As the Cr-bearing phase has a higher corrosion resistance, when immersed in nitric acid, the Ni−Mg phase is etched away and the Fe−Cr phase remains as a connected, spongelike porous structure. After immersion in 3 M nitric acid, the ribbon sample completes its transformation from the precursor sheet into the final Fe−Cr bicontinuous nanoporous structures, which are studied in this work later. A schematic of the dealloying process is shown in Figure S1 (Supporting Information).

We note that the dealloying process does not require the high-temperature treatment and has been demonstrated to form a similar bicontinuous structure under lower-temperature conditions.[42] In general terms, considering the case with binary precursor alloy A−B and metallic metal phase C (metallic melt), when mixing enthalpy is negative between liquid metal C and the miscible phase B, phase B will be dissolved into phase C, whereas other immiscible phase A with positive enthalpy remains and spontaneously forms a connected structure. The solidification of the liquid metal post dealloying leads to the formation of a composite, with an A-rich phase and a B−C solid phase. After etching, the composite that contains the miscible phase (B) is then removed, and a nanoporous structure with enriched A phase is achieved.[27,42]

A total of 15 samples were prepared under different controlled conditions to cover the processing parameters of interest. All of the

DOI: 10.1021/acsami.7b04659
ACS Appl. Mater. Interfaces 2017, 9, 34172−34184

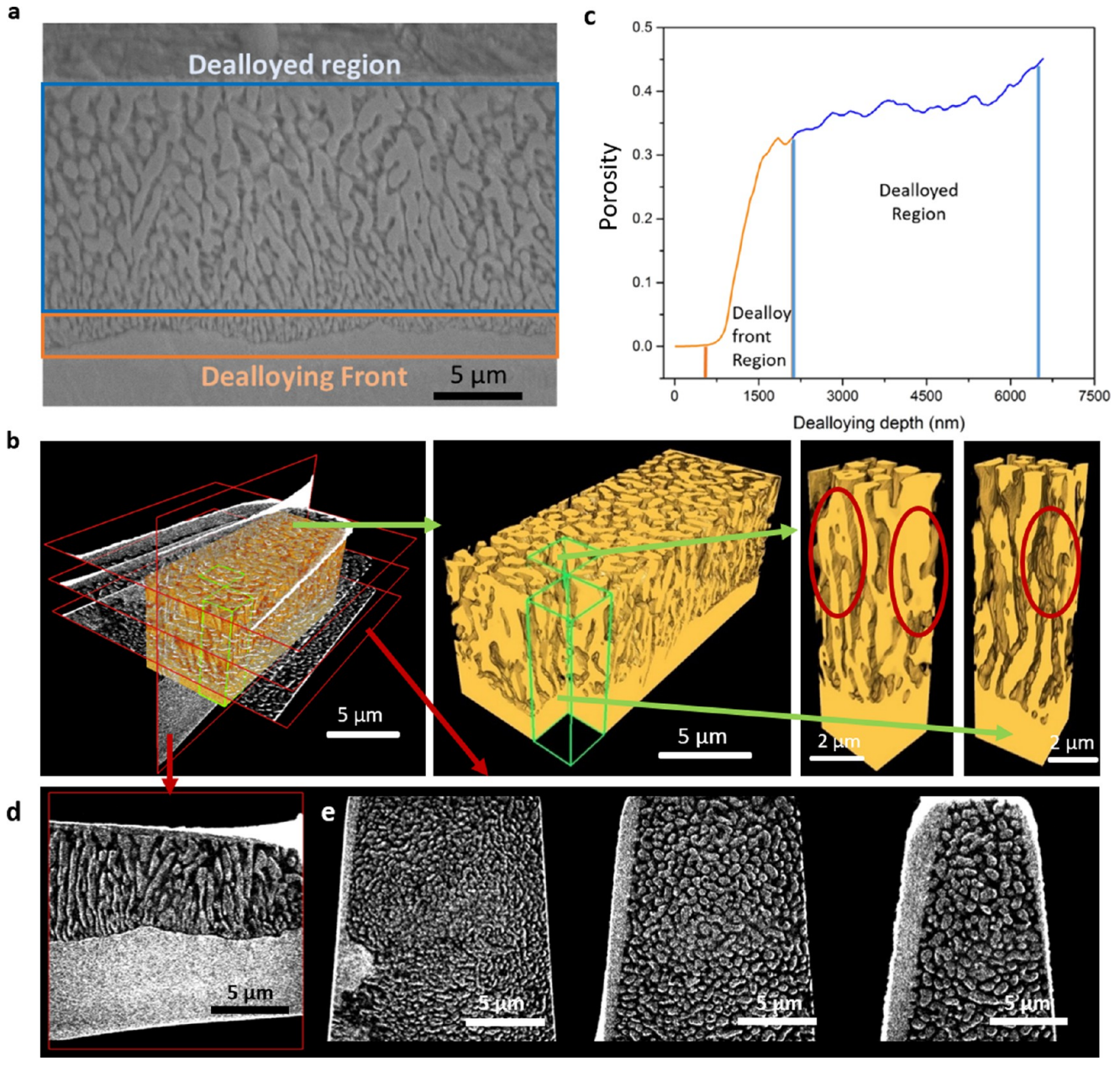

Figure 1. Morphology evolution at the liquid metal dealloying front, from dealloying a $(Fe_{0.8}Cr_{0.2})_{50}Ni_{50}$ precursor for 1 min at 973 K. (a) Two-dimensional SEM images showing ligament-size and pore-size gradients along the dealloying direction. (b) An X-ray nanotomography reconstruction showing its 3D morphology. (c) Quantification of porosity evolution with dealloying depth. Pseudo-cross sections from X-ray nanotomography showing the dealloying front: parallel (d) and perpendicular (e) to the dealloying direction.

samples studied in this work are listed in Table S1 (Supporting Information). The surfaces of the samples were examined by SEM. For X-ray nanotomography measurements, nanoporous Fe−Cr sample sheets were cut into a wedge shape with a tip of about 50 μm, sized to fit into the transmission X-ray microscopy field of view by razor blades and mounted onto a pin by epoxy. All 15 samples were measured by X-ray nanotomography to investigate the processing parameters of precursor composition, dealloying time, and dealloying temperature. For XRF analysis, the samples were directly fastened to the sample holder by applying a small quantity of adhesives at the corners.

In addition to thin samples, bulk samples were prepared to study the cross sections by SEM. The bulk samples were disk-shaped with 1 cm diameter and 1 mm thickness. The bulk samples were prepared by submerging the $(Fe_{0.8}Cr_{0.2})_{50}Ni_{50}$ precursor in the Mg melt and dealloying it at 973 K for 1, 5, and 10 min. A diamond saw was used to cut the sample in half. The cross sections of the samples were then polished and examined by SEM.

2.2. X-ray Microscopy Characterization. Synchrotron X-ray nanotomography measurements were conducted using transmission X-ray microscope beamline 32-ID-C at Advanced Photon Source (Argonne National Laboratory, Argonne).[43] A beam-shaping condenser[44] was used to illuminate the sample, and an objective zone plate with 60 nm outermost zone width was used to form an absorption contrast projection image in a charge-coupled device camera (with the sensor segmented into 2160 × 2560 pixels). To ensure that a sample stays within the X-ray field of view, an optical objective lens of either 10 times (10×) or 5 times (5×) magnification was used, which corresponds to a field of view of 26 × 31 μm^2 (10×) or 52 × 62 μm^2 (5×). For each sample under each dealloying condition, 1201 projections were collected over a 180° angular range, each of which was exposed for 2 s, with the angular step size of 0.15°.

DOI: 10.1021/acsami.7b04659
ACS Appl. Mater. Interfaces 2017, 9, 34172−34184

The sample was illuminated with a monochromatic X-ray beam of 7.112 keV.

Microbeam X-ray fluorescence (μ-XRF) imaging was conducted using submicron resolution X-ray spectroscopy (SRX) beamline at 5-ID,[45] National Synchrotron Light Source II, Brookhaven National Laboratory (BNL). A beam focus of ~1 × 1 μm^2 was created by a set of Kirkpatrick–Baez focusing mirrors at the sample position. Two-dimensional XRF imaging was conducted by raster scanning the sample relative to the X-ray beam, with incident X-ray energy of 9 keV. At each scanning point on the sample, a fluorescence spectrum was recorded by a silicon drift detector with a dwell time for one point set to 0.3 s. The scanning step size between each point for coarse scanning was set to 2 or 4 μm, and for fine scanning, 0.5 or 1 μm, depending on studying the composition of local features or on larger areas. Scanning area was set to 160 × 160 μm^2 for 4 μm step size coarsening scanning and 40 × 40 μm^2 for 1 μm scanning.

The sample formed from the precursor, $(Fe_{0.8}Cr_{0.2})_{50}Ni_{50}$, dealloyed after 1 min at 973 K, was prepared with an FIB lift-out procedure[46] to extract the dealloying front region. The sample was then imaged by a laboratory nanotomography instrument produced by Carl Zeiss, a ZEISS Xradia 810 Ultra. A total of 901 projects were collected with absorption contrast at 5.4 keV and an exposure time of 60 s per projection. The instrument provides a 2D resolution of 50 nm with a 16 μm field of view.

Therefore, X-ray nanotomography enabled studying the 3D structure of both the initial dealloying morphology around the dealloying front and the quantitative information on the coarser structure at the later stage of processing. Energy-dispersive X-ray spectroscopy (EDS) has shown Ni residue in the final np-ss structure below the detection limit of EDS[27] but was unable to reveal the detailed spatial distribution of the residual phase.

2.3. Data Processing and Analysis. For X-ray nanotomography analysis, a filtered back-projection algorithm was applied to reconstruct each tomographic data set with a Python-based software package TomoPy.[43,47−52] Smoothing and thresholding segmentation were applied on the reconstructed image in Image J[53] (see Supporting Information for details). On the basis of 3D images and customized Matlab codes developed in-house at BNL, various morphology parameters can be extracted, including average tortuosity, pore size distribution, average pore size, curvature, and interfacial shape.[54] The algorithm for tortuosity calculation used the neighboring method under the "quasi-Euclidean definition".[55] The curvature analysis was carried out using software Avizo (9.0 FEI) and programs developed by the authors in Matlab, following well-established methods in the literature.[39,56,57]

For XRF analysis, fluorescence spectrum fitting was performed using PyXRF,[58] an X-ray fluorescence analysis package developed at NSLS-II. We first fit the summed spectrum over the entire measurement area according to the nonlinear least-squares method[59] to determine global parameters, such as typical peak width, energy calibration, and parameters related to the contribution of Compton and elastic peaks in the data acquired at each point. After obtaining the correct global parameters, we applied single pixel fitting to fit the peak area of each element using a nonnegative least-squares method.[60] A Python library for multiprocessing has been implemented in this package. After obtaining maps of individual elements, including Fe, Cr, and Ni, further analysis to extract the residual Ni concentration and elemental correlation was conducted with custom programming in Python and Smak[61] software environments. The sum of the peak area from the XRF spectra over all sample measurement points is used to represent the overall elemental quantity. To avoid artifacts from morphological effects, the quantity of Ni was normalized against the quantity of Fe for a fairer comparison between samples. We note that the detected depth is estimated to be approximately 30−50 μm from the surface of the sample into its bulk. This calculation takes into account that the porosity of the materials, the attenuation length of the X-rays in this material at a 9 keV X-ray energy, and the self-absorption of the emitted, fluorescent X-rays.

3. RESULTS AND DISCUSSION

3.1. Morphology of Nanoporous Stainless Steel at Dealloying Front. Both 2D cross-sectional SEM and 3D X-ray nanotomography were conducted to study the morphology of the np-ss at the dealloying front, corresponding to the early dealloying stage. A feature-size gradient and the dealloying direction can be observed in the cross-sectional SEM, as shown in Figure 1a. At the dealloying front, ligaments that elongate along the dealloying direction, roughly perpendicular to the dealloying interface, can be observed. Both phenomena, ligament-size and pore-size gradients and the elongation of ligaments at the dealloying front, shown in Figure 1b, were also observed in the solid–solid diffusion of the same steel materials system previously characterized by Wada et al.[42] McCue et al. characterized another liquid metal dealloying system, Ti–Ta alloys immersed in molten Cu,[33] and also reported a well-connected structure in the SEM analysis. However, this morphology at the dealloying front differs slightly in topology and morphology when compared with work done by Geslin et al.[34] as discussed below.

Geslin et al.[34] simulated the topological evolution near a dealloying front in a Ti–Ta–Cu system, with lamellar (2D) and filamentary (3D) morphologies similar to those observed here. However, in their work, these lamellar and filamentary structures were only observed at lower immiscible element concentration (25% for 2D and <25% for 3D). At a higher immiscible element concentration (>25%), they observed a well-connected, nonlamellar structure at the dealloying front in their simulation. In comparison, we still observed the filamentary structure in 3D with a relatively high immiscible phase (50 atom %) in the system. The elongation of the ligaments can be clearly observed in our results, nearly resembling the "lamellar" structure, as shown in the 2D simulation. This difference may be attributed to the elemental differences in the studied systems. This also suggests that further simulation/theoretical work may still be required to fully understand the complex nature of the liquid metal dealloying. In particular, there is a need to addressing the dimensionality effects, which result in differences in the 2D and 3D morphologies near the dealloying front.

On the basis of the 3D reconstruction of the dealloying front, we characterized the porosity evolution along the dealloying depth, the displacement along the dealloying direction, which is shown in Figure 1c. We note that the dealloying front is not a flat surface experimentally, a character that it may have inherited from the surface flatness of the sample. At the dealloying front, the dealloyed region is mixed with the undealloyed region and therefore the porosity significantly varies with dealloying depth. As a result of simultaneous coarsening, the ligament size increased, whereas the porosity was not influenced, which resulted in a relative constant porosity at ~2000 nm away from the dealloying front. However, the porosity still slightly increased in this dealloyed region, which can be explained as an unfinished dealloying process, and corresponds to the results shown in the next section. The porosity at the dealloyed region, further away from the dealloying front, is close to the result in the ribbon sample, which will be reported in the next section. We note that in both SEM and X-ray nanotomography reconstructions, a discontinuity between the tip of ligaments and the undealloyed region was observed. This may be attributed to a structural instability due to the high surface energy on the as-dealloyed interface and

DOI: 10.1021/acsami.7b04659
ACS Appl. Mater. Interfaces 2017, 9, 34172−34184

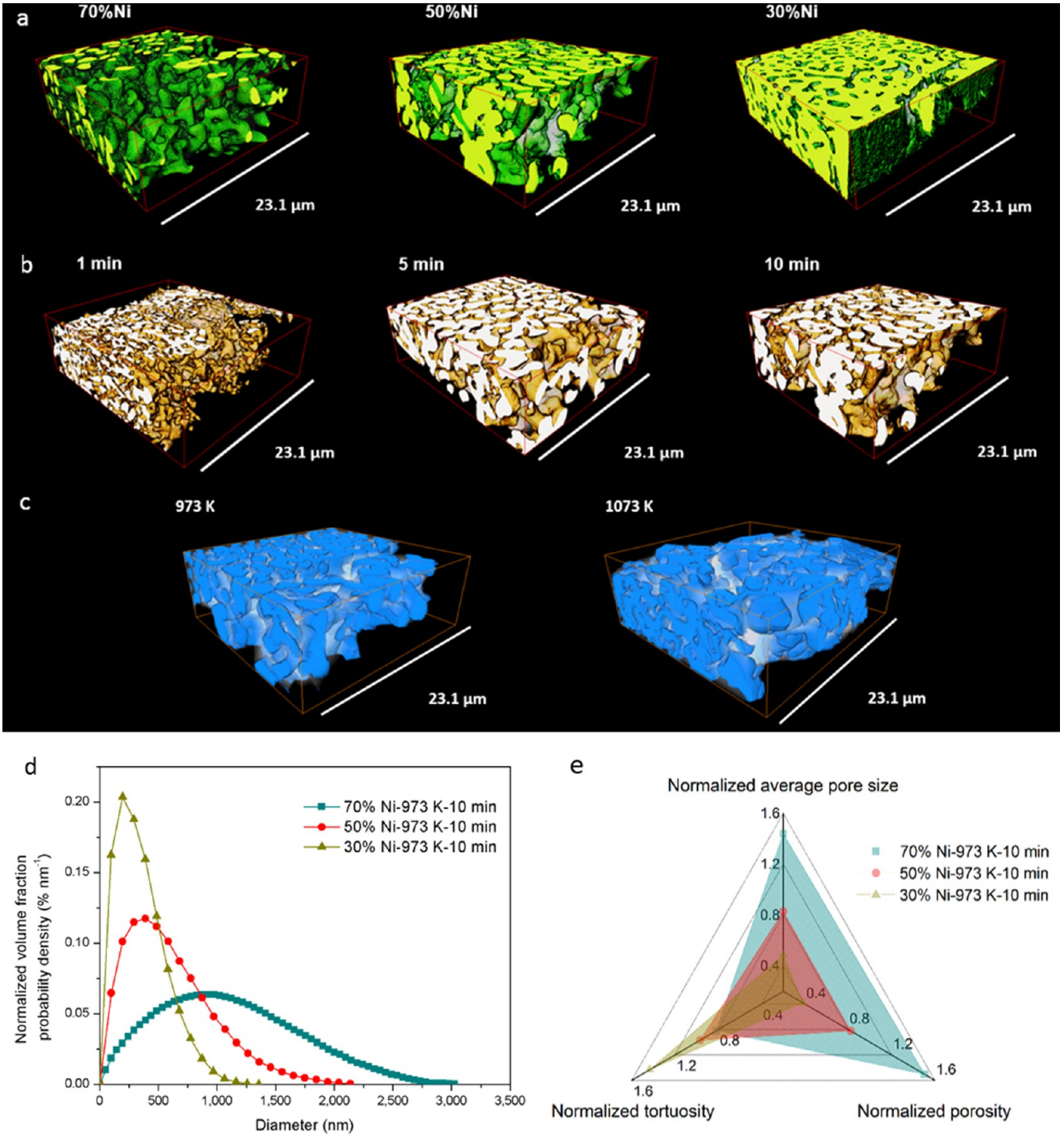

Figure 2. Three-dimensional reconstructions of np-ss samples and their quantitative analysis. Three-dimensional reconstructions of nanoporous stainless steel fabricated from (a) precursor $(Fe_{0.8}Cr_{0.2})_{1-x}Ni_x$, x = 70, 50, and 30%, dealloyed for 1 min in 973 K Mg melt; (b) $(Fe_{0.8}Cr_{0.2})_{30}Ni_{70}$ for 1, 5, and 10 min in 973 K Mg melt; (c) $(Fe_{0.8}Cr_{0.2})_{30}Ni_{70}$, dealloyed for 1 min in 973 and 1073 K Mg melt. (d, e) Three-dimensional quantitative analyses of three different precursor compositions, $(Fe_{0.8}Cr_{0.2})_{1-x}Ni_x$, x = 30, 50, and 70%, at fixed dealloying time (10 min) and temperature (973 K): (d) pore size distribution and (e) the normalized porosity, tortuosity, and average pore size.

a subsequent coarsening. This is consistent with the 2D SEM image presented by Wada et al.;[42] however, it has not been reported previously. Pseudo-cross sections from the X-ray nanotomography showing the morphology of dealloying front are also presented, with Figure 1d showing the direction parallel to the dealloying direction and Figure 1e showing the direction perpendicular to the dealloying direction. The elongation of ligaments, which is a structure with lower tortuosity, is also beneficial for materials transportation through the porous structure. This has been previously demonstrated by artificially engineered battery electrodes.[62] Here, a low-tortuosity structure can be dynamically formed during the self-organizing material synthesis.

Overall, the larger feature size, the ligament/pore size gradient, and the lamellar structure are characteristically different from the porous structures fabricated by aqueous

DOI: 10.1021/acsami.7b04659
ACS Appl. Mater. Interfaces 2017, 9, 34172−34184

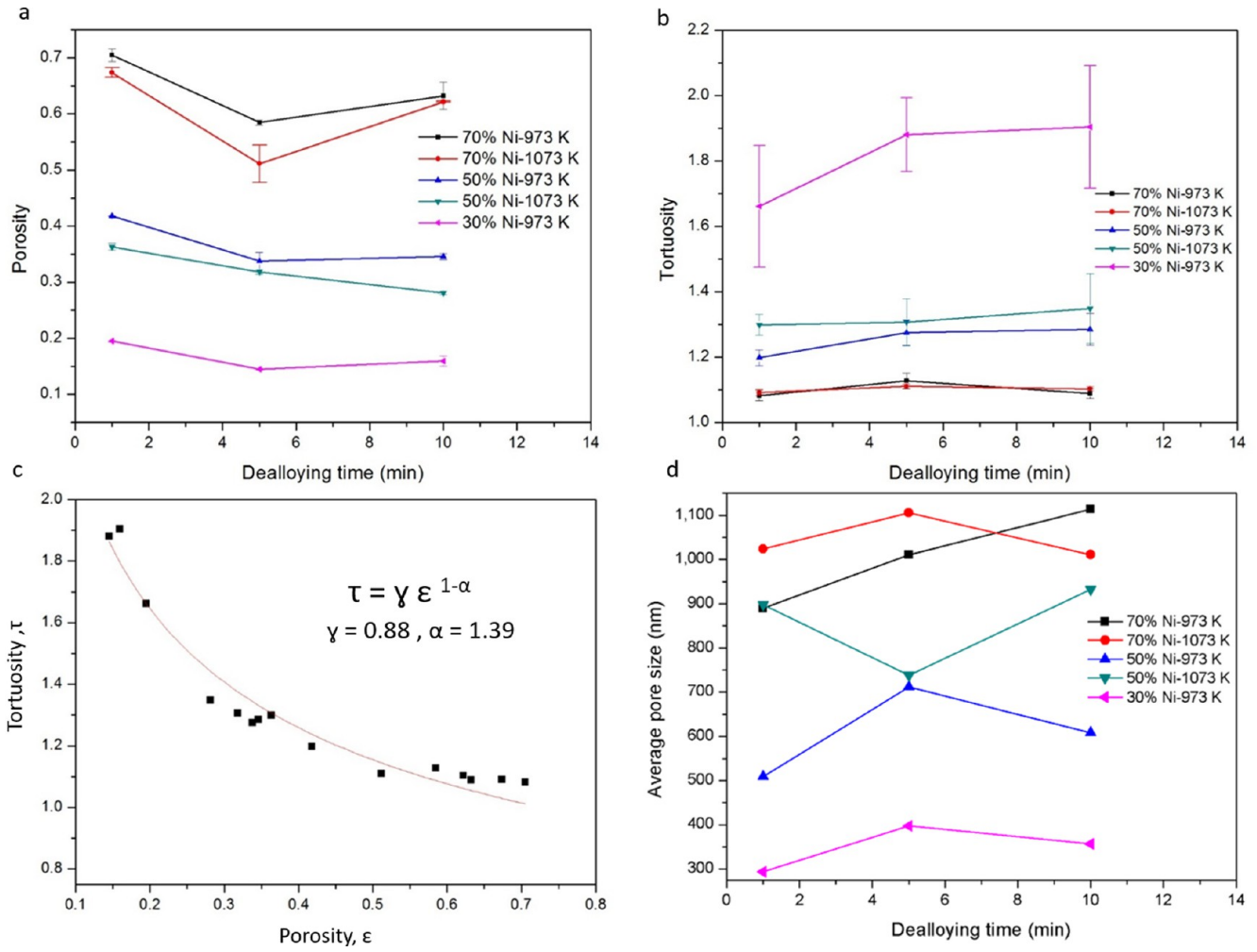

Figure 3. Critical 3D morphological properties vs dealloying time, temperature, and precursor composition: (a) porosity, (b) tortuosity, (c) relationship between porosity and tortuosity fitted with a generalized Bruggeman relationship, and (d) average pore size are displayed.

dealloying. Compared to aqueous solution dealloying, liquid metal dealloying uses a process with higher temperature; the temperature needs to be higher than the melting temperature of the dealloying agent to create a molten metal bath. This leads to a faster simultaneous coarsening of the structure during the dealloying process. In aqueous dealloying, the porous structure is relatively homogeneous, and the ligament size before the heat treatment is around 3−20 nm,[36−38] tunable to microns by additional heat treatment via isothermal annealing.[39] For liquid metal dealloying, the size of ligament was in nanometer length scale at the dealloying front, as seen here, beyond the transmission X-ray microscopy resolution (30 nm). The simultaneous coarsening of the ligaments during the high-temperature dealloying leads to a larger size distribution (hundreds of nanometers to microns) and ligament-size and pore-size gradients along the dealloying direction. To alleviate coarsening among ligaments in the Ti−Ta−Cu system, McCue et al. added Ag and Bi into the Cu metallic melt to lower the dealloying temperature.[33] In addition, solid-state interfacial dealloying, replacing metallic melt by a metal sheet, was demonstrated to fabricate the bicontinuous structure at a lower temperature and to control the ligament size down to 1 order of magnitude finer.[42] The lamellar structure near the dealloying front is also a unique character of the liquid metal dealloying; similar structure has not yet been observed in aqueous solution dealloying. This may be because of the different kinetics processes, or the finer length scale in aqueous dealloying limits the ability to observe such structure at the dealloying front. This pore-size gradient observed in the np-ss prepared by liquid metal dealloying can be a material design feature and to be explored in future applications. In addition, future studies are required to fully understand the kinetics in the liquid metal dealloying process, including the influence of grain size, grain orientation,[63,64] and acid temperature and type[65] on the final porous structure.

In the following section, we discuss the process−structure−property relationship of samples that have been dealloyed sufficiently to resemble the well-connected, stable structure required for practical applications. The structure differs from the high-gradient, lamellar early dealloyed structure discussed here. The extent of the dealloying depth in 2D is 80 μm on one side, as shown in Figure S13 (Supporting Information), whereas the total thickness of the ribbon sample is around 100 μm. When the ribbon is immersed in the melt, dealloying will occur from both sides and the entire precursor will be dealloyed and experience coarsening. In coarsening, two processes, including surface smoothening and ligament pinch-off events, are involved,[66,67] which leads to a relatively more random and isotropic structure at the dealloyed region

DOI: 10.1021/acsami.7b04659
ACS Appl. Mater. Interfaces 2017, 9, 34172−34184

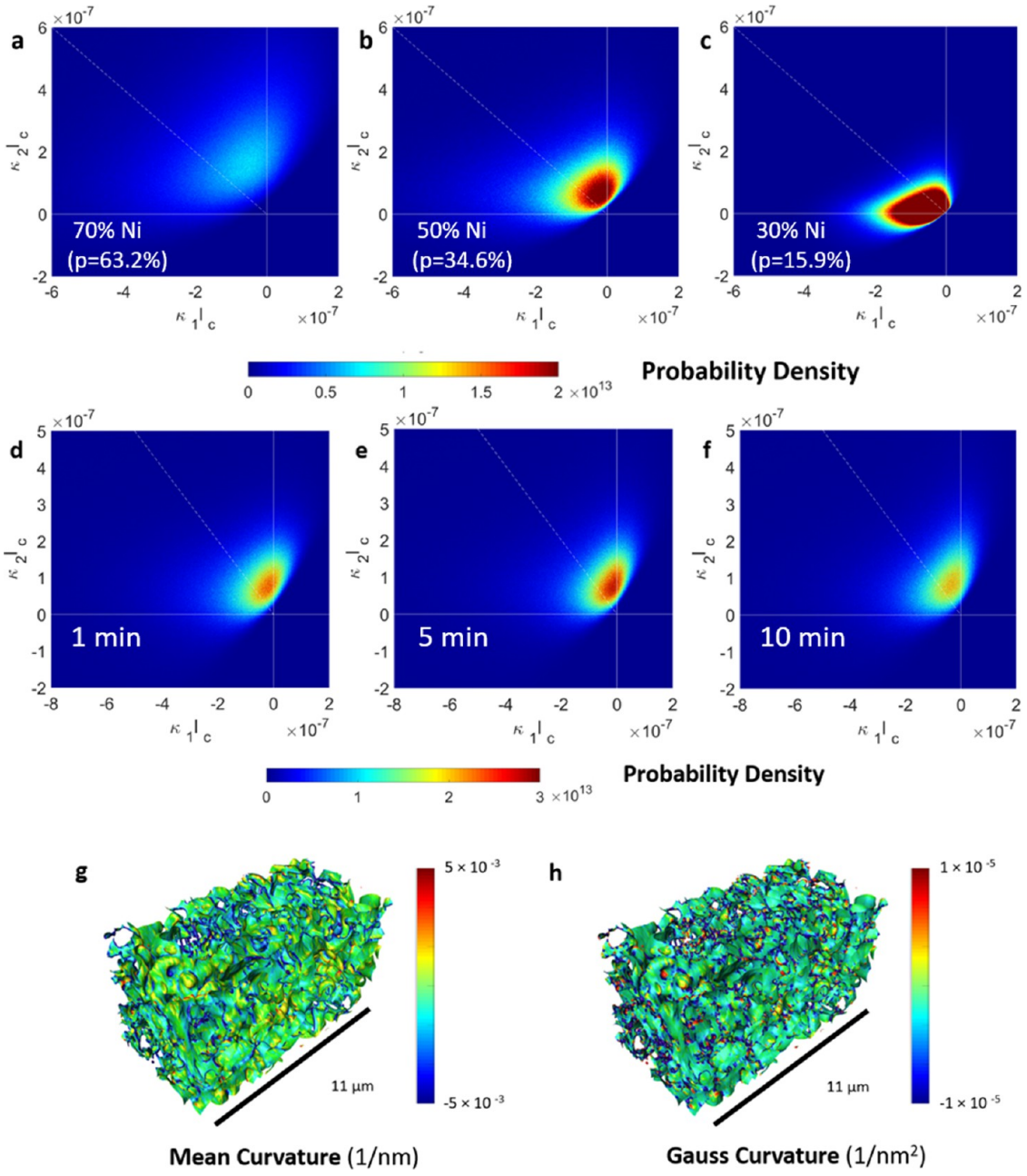

Figure 4. Shape analysis of nanoporous stainless steels. (a–c) Interfacial shape distributions (ISDs) of samples with precursor $(Fe_{0.8}Cr_{0.2})_{1-x}Ni_x$, x = 70, 50, and 30 atom %, dealloyed 10 min at 973 K. The porosities (p) of the corresponding samples are 63.2, 34.6, and 15.9%. (d–f) ISDs of samples with precursor $(Fe_{0.8}Cr_{0.2})_{50}Ni_{50}$, dealloyed 1, 5, and 10 min at 1073 K. (g, h) Mean and Gaussian curvatures in the sample with 50% Ni in precursor, dealloyed 1 min at 1073 K.

compared to the dealloying front. The longer coarsening time leads to larger ligaments and less anisotropy.

3.2. Three-Dimensional Morphological Evolution from X-ray Nanotomography. The morphological evolution with precursor compositions, dealloying time, and dealloying temperature was studied. Figure 2a–c shows the 3D reconstructions from X-ray nanotomography of np-ss samples, fabricated from precursor $(Fe_{0.8}Cr_{0.2})_{1-x}Ni_x$, x = 30, 50, and 70%, dealloyed for 1, 5, and 10 min, in 973 and 1073 K Mg melt. The corresponding SEM images are shown in Figure S4 (Supporting Information). Figure 2d shows our quantitative pore size distribution analysis. With a larger amount of Ni in the precursor, dealloying will result in larger pore sizes and wider pore size distributions. This can be attributed to the space freed from Ni removal after dealloying and the spontaneous coarsening of porous structure. It also indicates that relatively little densification occurred during the dealloying, coarsening, and etching processes. Quantification shows that dealloyed samples with 70% Ni in the precursor, the sample that produces the largest pore, will result in pores with diameter up to 3 μm.

A radar chart[68] presented in Figure 2e shows normalized morphological parameters, including average pore size, tortuosity, and porosity, for these three samples. It clearly visualizes the effect of Ni concentration in the precursor on the morphology in np-ss: the higher the Ni concentration (a value that ranges between 30 and 70% here), the higher the average pore size and porosity, and tortuosity is inversely correlated

DOI: 10.1021/acsami.7b04659
ACS Appl. Mater. Interfaces 2017, 9, 34172–34184

with the porosity. Similar visualizations for the influence of dealloying time and temperature can be found in the Supporting Information.

Porosity, tortuosity, and average pore size were quantified as a function of processing conditions. First, the porosity evolution under each precursor composition, dealloying temperature, and dealloying time is summarized in Figure 3a. The theoretical maximum porosity can be calculated on the basis of the known volume fraction (vol %), density of Ni, and the fact that dealloying $(Fe_{0.8}Cr_{0.2})_{1-x}Ni_x$ to form np-ss results in a phase transformation from FCC structure with a = 3.524 Å to BCC structure with a = 2.860 Å. A $(Fe_{0.8}Cr_{0.2})_{30}Ni_{70}$ precursor will yield a final product, $Fe_{0.8}Cr_{0.2}$, with a theoretical porosity of 67.9%, in contrast to 46.5% for the precursor $(Fe_{0.8}Cr_{0.2})_{50}Ni_{50}$ and 25.1% for $(Fe_{0.8}Cr_{0.2})_{70}Ni_{30}$. The measured porosity values from X-ray nanotomography are generally consistent with the expected theoretical value, but are slightly lower than theoretical values. This can be explained as due to either an incomplete dealloying process, as discussed in the XRF quantification section below, or densification accompanied with the dealloying process. The porosity measured here has an implication on permeability, another important property determining the behavior of gas and liquid flow in porous structures, critical for many applications. For the same size of the ligament structures, permeability increases with porosity. Therefore, in analogy, to achieve a higher permeability in np-ss, a higher nickel concentration in the precursor can be considered.

A trend of porosity evolution with dealloying time can be observed in Figure 3a, where porosity decreases with dealloying time initially, but then increases. This may be attributed to three competing mechanisms: dealloying, coarsening, and densification. Dealloying is expected to increase porosity; coarsening is expected to increase ligament and/or pore size, but does not affect porosity; and densification is expected to reduce porosity and pore size, thereby increasing ligament size. The combination of these three mechanisms can therefore lead to a complex porosity variation.

Porosity and tortuosity, important parameters controlling materials transport in porous structure, are not independent. The quantitative relationship between porosity and tortuosity shown in this work can provide a guideline in this respect. The Bruggeman relation has been successfully applied in different porous structures and shows a good predictive ability of the relationship between porosity or volume fraction and tortuosity.[69] Here, we compared different fitting models, including the Bruggeman model, generalized Bruggeman model,[70] and a generic diffusion and transportation model.[71,72] The generalized Bruggeman model shows the best fit in the np-ss, as shown in Figure 3c (see Figure S11 (Supporting Information) for the fitting results of the different models): $\tau = \gamma\varepsilon^{1-\alpha}$, where τ is the tortuosity and ε is the porosity, and γ and α are morphology-dependent fitting parameters. γ and α were determined to be 0.88 and 1.39 for the np-ss samples, respectively. In nanoporous titanium (np-Ti) samples fabricated also by liquid metal dealloying, tortuosity values are between 1.2 and 1.8, which are close to the np-ss tortuosity presented here. It was shown that the Bruggeman relation fits well with the np-Ti samples, which are slightly different from the np-ss case, indicating differences in morphology.[56] In nanoporous gold fabricated by electrochemical dealloying, the tortuosity in a 70% porosity sample is around 3,[73] which is significantly higher than the tortuosity in the np-ss and np-Ti. The lower tortuosity in the liquid metal dealloyed samples indicates a porous structure that is less tortuous than the one fabricated by electrochemical dealloying. This indicates some intrinsic differences in morphology between these two types of structure.

3.3. Curvature Analysis. To further quantify the morphology of nanoporous stainless steel, we applied a curvature analysis based on interfacial shape distribution (ISD).[74] An ISD reflects the probability of finding a patch on interface with a given pair of maximum and minimum principal curvatures. By measuring the ISD of np-ss samples, we quantitatively represented the interfacial shape between the stainless steel ligaments and the pores (or the surface of the ligaments). Figure 4a–c shows the ISDs of samples dealloyed from different precursor compositions; it also corresponds to samples with different porosities. Furthermore, the principal curvatures can be converted to a different way of representing the shape of the surface: the mean curvature, $H = (\kappa_1 + \kappa_2)/2$, and the Gaussian curvature, $K = \kappa_1\kappa_2$. The κ_1 and κ_2 divide the ISD into four quadrants: the surface patches with convex and concave shapes ($K > 0$) correspond to the points in the first and third quadrants, respectively, whereas the saddle or elliptical shapes ($K < 0$) locate in the second quadrant. The distribution falling on the $\kappa_1 = 0$ and $\kappa_2 = 0$ (white solid lines) represents patches on cylinder-shaped surface; the white dotted line refers to the zero mean curvature line, where $\kappa_1 = -\kappa_2$. We note that all of the curvature values here have been scaled with average ligament sizes so that the distributions solely depend on the interfacial shape and not on the size of the ligaments. The horizontal and vertical axes in the ISDs correspond to the minimum (κ_1) and maximum principal curvatures (κ_2), respectively.

As can be seen in Figure 4a,b, with 50 and 70% of Ni in the precursor, the ISDs of the resulting np-ss mostly fall in the second quadrants; small portion of the ISDs falls in the first quadrants, and very small portion falls in the third quadrants. This indicates that the saddle shape is the dominant shape in these porous stainless steels. First, these ISDs of np-ss are similar to the ISDs of the nanoporous Ti, also fabricated by the liquid metal dealloying.[56] More interestingly, the ISDs of np-ss are also qualitatively similar to the ISDs of nanoporous gold, indicating that the shapes in these two types of samples are similar in nature.[39,75]

Overall, there is a shift in the ISDs of np-ss toward the third quadrants when the porosity is decreasing in the np-ss samples. Noticeably, 30% Ni sample has a significantly different morphology, as represented by the ISD in Figure 4c. In comparison with Figure 4a,b, this ISD shows a higher probability density around the $\kappa_1 = 0$ line and also in the third quadrant, which indicates an interfacial shape consisting of cylindrical shapes with concave ends, in addition to the saddle points. This morphological transition from 70 and 50% Ni samples to 30% Ni samples can also be observed visually in Figure 2a–c. Here, we observed an interfacial shape transition from a classic bicontinuous shape, which is dominated by saddle-shaped interfaces, toward a channel-like porous structure, due to the lowering of the porosity from 63.2 to 15.9%. This type of structure was not observed in nanoporous gold because the partition limit was determined to be ~40 atom % of Ag in the Ag–Au alloy.[35]

The ISDs in Figure 4d–f then represent the ligament–pore interfacial shape with different dealloying times. The simultaneous coarsening and densification are expected to play a more

DOI: 10.1021/acsami.7b04659
ACS Appl. Mater. Interfaces 2017, 9, 34172–34184

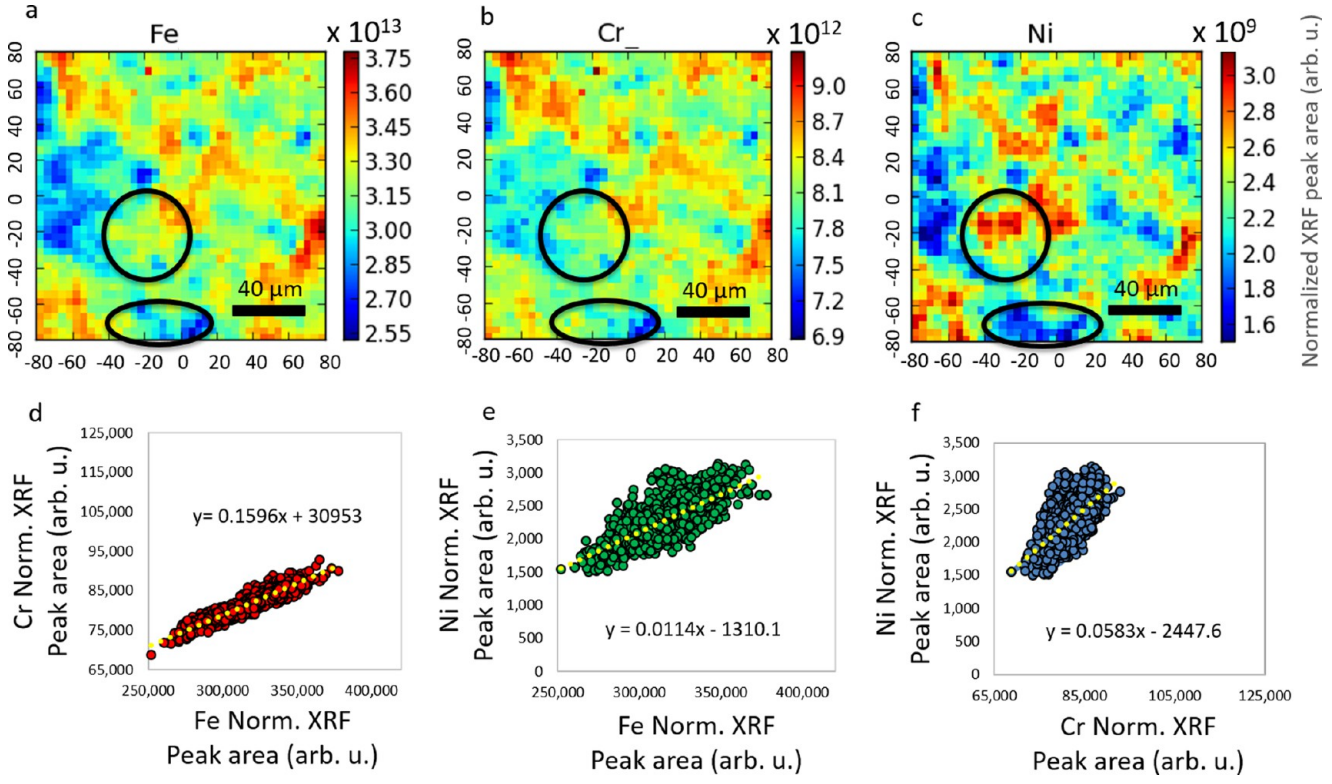

Figure 5. $(Fe_{0.8}Cr_{0.2})_{30}Ni_{70}$ dealloyed 1 min in 973 K Mg Melt. (a–c) Two-dimensional element maps of Fe, Cr, and Ni. Circled regions show locations where Ni and Fe–Cr alloy are not positively correlated, indicating heterogeneity. (d–f) Fe–Cr, Fe–Ni, and Cr–Ni correlations.

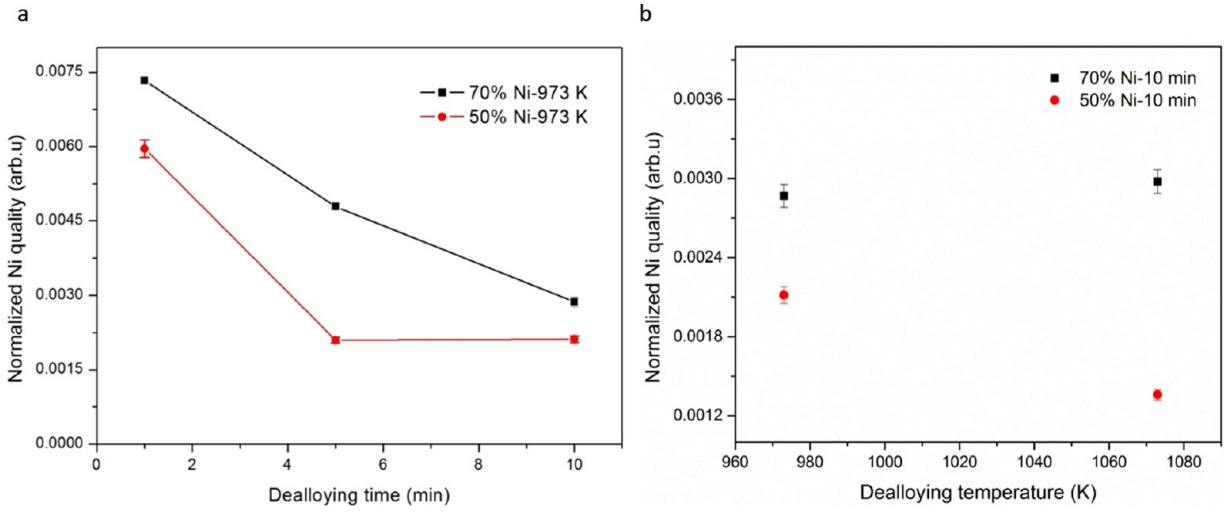

Figure 6. Residue Ni evolution with (a) dealloying time and (b) dealloying temperature.

critical role in the morphological evolution of the np-ss than in the nanoporous gold. The different rates of ligament-size increase and curvature decreases as a result of coarsening and densification may influence the shape of the samples, represented by the ISDs. However, there is no significant ISD change between samples with different dealloying times. Nevertheless, the slight probability distribution change in the ISDs indicates that the morphological evolution of liquid metal dealloying did not progress completely in a self-similar manner.

The mean and Gaussian curvature distributions on the porous structure are shown in Figure 4g,h. Consistent with the representation of ISDs, a large fraction of the ligament–pore interface exhibits a saddle shape with the mean curvature values close to zero and slightly negative Gaussian curvature values. Only at the tip of ligaments, the mean and Gaussian curvatures are positive.

3.4. Elemental Distribution and Residual Evolution Quantified by X-ray Fluorescence Microscopy. A representative result of element analysis based on XRF microscopy is shown in Figure 5. The distribution of the elements contained in the sample is shown in Figure 5a–c. The degree of compositional homogeneity can be quantified by plotting the correlation between elements, using quantities of elements at each pixel, that is, scanned position. The correlation figures for Cr versus Fe, Ni versus Fe, and Cr versus Ni are shown in Figure 5d–f, respectively. The quantities are

DOI: 10.1021/acsami.7b04659
ACS Appl. Mater. Interfaces 2017, 9, 34172–34184

estimated from the area of the peak in the XRF spectra corresponding to each element.

The Fe and Cr distributions in the sample are positively correlated with each other with a narrow distribution, as expected for the homogeneous stainless steel phase. The correlation between the residue element Ni with the main np-ss phase shows a wider distribution; Fe−Ni and Ni−Cr correlate not as well as Fe−Cr, indicating a slightly inhomogeneous Ni distribution. This is shown in the circled regions in Figure 5a−c. XRF microscopy was used to verify the homogeneity of the precursors (see further results in the Supporting Information), and this slight difference attributes to the dealloying process. Other samples present similar elemental distributions, showing the existence of the Fe−Cr phase as indicated by the consistent Fe−Cr linear correlation, with a small amount of Ni residue, showing little heterogeneity; after dealloying $(Fe_{0.8}Cr_{0.2})_{30}Ni_{70}$ 1 min under 973 K, the Ni concentration was 0.76 ± 0.07 atom %, as determined by EDX in SEM.

It is therefore of interest to analyze the amount of Ni residual in the samples. Figure 6a shows that the quantity of Ni evolves as a function of the dealloying time. The Ni-to-Fe ratio continues to decrease, which reflects the continuation of the dealloying process after 5 min. In the 70% Ni samples, the residual Ni concentration continues to diminish with longer dealloying time. However, in the 50% Ni samples, the Ni concentration remains constant after 5 min of dealloying. This indicates that the dealloying mechanism is no longer capable of causing further phase separation under these environmental conditions at the residual Ni concentration. However, this limiting value depends on dealloying condition. For example, when the temperature shifts, a different limiting residual Ni value may be reached, as shown in Figure 6b.

In np-ss prepared from a 50% Ni precursor, the limiting Ni residue value is further reduced for higher dealloying temperatures, here at 1073 K. It should be noted that a quantitative comparison of the elemental quantity in 70% Ni versus 50% Ni samples can be misleading due to the different amount of X-ray self-absorption. For instance, 50% samples have lower porosity and thus higher Fe−Cr density for a given sample volume; therefore, the Ni fluorescence signal has a higher probability to be absorbed by the Fe−Cr of the structure, resulting in an underestimated Ni quantity due to this self-absorption. Nevertheless, comparing elemental quantities for samples with the same precursor composition remains valid because they have similar porosities and self-absorption effects.

The residual elements can play a critical role in applications, where the functionalities are determined by the surface composition, such as catalysis. This can be used as a feature to design and tailor the material for specific catalytic properties. Similarly, elemental residuals were also discovered from the aqueous dealloying.[40] Further analysis is required to truly establish the characteristics of these residual elements in samples fabricated by the liquid metal dealloying. Additional dealloying temperature also needs to be tested in the future to further understand the kinetics of the dealloying process and the simultaneous coarsening and density, all of which control the resulting 3D morphology, elemental residue, and therefore the properties of the porous materials.

4. CONCLUSIONS

We investigated the dealloying of $(Fe_{0.8}Cr_{0.2})_{1-x}Ni_x$ alloy (x = 30, 50, and 70 atom %) by liquid metal dealloying, with Mg metallic melt. The 3D morphology at the dealloying front was first characterized by X-ray nanotomography, showing elongated ligaments; the ligaments are approximately perpendicular to the dealloying front. This unique structure has not been observed in samples prepared by dealloying in an aqueous solution. The simultaneous coarsening also more pronouncedly affects the material morphology at this early dealloying stage, leading to pore-size and ligament-size gradients. Furthermore, the 3D morphology and elemental distribution of nanoporous stainless steels at a later dealloying stage were studied as a function of precursor compositions, dealloying time, and dealloying temperature. X-ray nanotomography provides a direct visualization of the complex, 3D bicontinuous structure. The critical 3D morphological parameters, including pore size distribution, tortuosity, porosity, average pore size, curvature, and interfacial shape, were quantified. Precursor composition was quantified to be the most direct controlling parameter in comparison with dealloying time and temperature, determining porous morphology. We also discussed the morphological differences between np-ss samples prepared by the liquid metal dealloying and nanoporous gold samples prepared by aqueous dealloying. Importantly, for the liquid metal dealloying, 3D morphological parameters are controlled by dealloying, coarsening, and densifications mechanisms, and the thickness of the samples will also influence morphological evolution with these mechanisms, developing pore-size and ligament-size gradients. The average pore size, porosity, and tortuosity correlate well with each other, where the generalized Bruggeman equation can be used to predict tortuosity from known porosity. Curvature analysis with ISDs quantitatively represents the shape of the np-ss, indicating a morphological transition from a classic bicontinuous structure to a channel-like porous structure, when the porosity in the sample decreases as controlled by the precursor composition. In addition, because coarsening and densification contribute to the porosity and size changes in samples with different dealloying times, the slight probability distribution change in their corresponding ISDs indicates that the morphological evolution of liquid metal dealloying did not progress completely in a self-similar manner, but the differences are only subtle. Fluorescence mapping results confirm the compositional evolution during the dealloying process and provide critical information on Ni residue quantification and elemental heterogeneity. Ni residue was found to lower with dealloying time until a limiting Ni concentration is reached. The majority of the samples were found to have a homogeneous Fe−Cr phase, proven by a direct positive correlation of these two elements, where Ni residues possess a slightly different spatial distribution. In the future, complementary porosity and pore size distribution by bulk methods, such as the Brunauer−Emmett−Teller (BET) method and/or mercury intrusion porosimetry, can be conducted and compared with the 3D nanotomography results. Additional work, particularly in situ measurements, can be conducted to further understand the role of dealloying and etching in determining the morphological evolution, dealloying front propagation, dealloying depth, as well as chemical compositions in liquid metal dealloying.

■ ASSOCIATED CONTENT

Supporting Information

The Supporting Information is available free of charge on the ACS Publications website at DOI: 10.1021/acsami.7b04659.

DOI: 10.1021/acsami.7b04659
ACS Appl. Mater. Interfaces 2017, 9, 34172−34184

Further details on experiments and analysis, including (1) the 3D morphology evolution as a function of dealloying time and temperature, (2) the correlation between different 3D morphological properties, (3) image-processing details, and (4) the relationship between morphological parameters and transportation properties (PDF)

AUTHOR INFORMATION

Corresponding Author

*E-mail: karen.chen-wiegart@stonybrook.edu.

ORCID

Chonghang Zhao: 0000-0002-3538-6199

Author Contributions

Y.-c.K.C.-W. and H.K. developed the research idea. T.W. prepared the np-ss samples under H.K.'s supervision. Y.-c.K.C.-W. wrote the general user proposals for the use of beamtime at APS and NSLS-II. V.D.A. built the transmission X-ray microscopy beamline at APS. V.D.A. set up the X-ray nanotomography experiment. C.Z. and Y.-c.K.C.-W. prepared the samples for nanotomography. C.Z., V.D.A., and Y.-c.K.C.-W. conducted the X-ray nanotomography experiment at APS and reconstructed the images. J.T. and V.D.A. designed the SRX beamline. J.T., G.W., and Y.-c.K.C.-W. commissioned the SRX beamline and setup for the XRF experiment. C.Z., G.W., Y.-c.K.C.-W., and J.T. conducted the XRF experiments. J.G. collected the dealloying-front X-ray nanotomography data. L.L. developed the software for XRF analysis. C.Z. processed the X-ray nanotomography and XRF data under Y.-c.K.C.-W.'s supervision. C.Z., Y.-c.K.C.-W., T.W., and H.K. discussed and interpreted the results, with inputs from other coauthors. C.Z. established the relationship between the morphological parameters with the properties of the devices, C.Z. and Y.-c.K.C.-W. wrote the manuscript with inputs from other coauthors.

Notes

The authors declare no competing financial interest.

ACKNOWLEDGMENTS

The authors thank Gwen Wright (Center for Functional Nanomaterials, CFN) for assisting SEM, and Fernando Camino (CFN) for EDS support and sample preparation with FIB-SEM. Doğa Gürsoy and Francesco De Carlo (Advance Photon Sources, APS) are acknowledged for support in X-ray tomography reconstruction software, TomoPy. Li Li (National Synchrotron Light Source II, NSLS-II) is acknowledged for the development of XRF analysis software, PyXRF. The development of PyXRF software was supported by LDRD grant, funded by Brookhaven National Laboratory, and we acknowledge the funding support and the collaboration with Yong Chu (NSLS-II), the principal investigator of the project. The authors are also very grateful to the technical support from James Biancarosa, Michael Maklary, Carey Koleda (NSLS-II), and Alex Deriy (APS); control support from Wayne Lewis and Tommy Tang; and mechanical and design support from Yuan Yao, Michael Lucas, and Richard Gambella (NSLS-II). This research used resources and Submicron Resolution X-ray Spectroscopy Beamline (SRX, 5-ID) of the National Synchrotron Light Source II, a U.S. Department of Energy (DOE) Office of Science User Facility operated for the DOE Office of Science by Brookhaven National Laboratory under Contract No. DE-SC0012704. This research used resources of the Advanced Photon Source, a U.S. Department of Energy (DOE) Office of Science User Facility operated for the DOE Office of Science by Argonne National Laboratory under Contract No. DE-AC02-06CH11357. K. Chen-Wiegart acknowledges support by the Department of Materials Science and Chemical Engineering, the College of Engineering and Applied Sciences, and the Stony Brook University, as well as by the Brookhaven National Laboratory under Contract No. DE-SC0012704.

REFERENCES

(1) Kränzlin, N.; Niederberger, M. Controlled Fabrication of Porous Metals From the Nanometer to the Macroscopic Scale. *Mater. Horiz.* **2015**, *2*, 359−377.

(2) Zhang, Z. H.; Wang, Y.; Qi, Z.; Zhang, W. H.; Qin, J. Y.; Frenzel, J. Generalized Fabrication of Nanoporous Metals (Au, Pd, Pt, Ag, and Cu) through Chemical Dealloying. *J. Phys. Chem. C* **2009**, *113*, 12629−12636.

(3) Xu, C.; Wang, R. Y.; Chen, M. W.; Zhang, Y.; Ding, Y. Dealloying to Nanoporous Au/Pt Alloys and their Structure Sensitive Electrocatalytic Properties. *Phys. Chem. Chem. Phys.* **2010**, *12*, 239−246.

(4) Sun, L.; Chien, C. L.; Searson, P. C. Fabrication of Nanoporous Nickel by Electrochemical Dealloying. *Chem. Mater.* **2004**, *16*, 3125−3129.

(5) Malgras, V.; Ji, Q. M.; Kamachi, Y.; Mori, T.; Shieh, F. K.; Wu, K. C. W.; Ariga, K.; Yamauchi, Y. Templated Synthesis for Nanoarchitectured Porous Materials. *Bull. Chem. Soc. Jpn.* **2015**, *88*, 1171−1200.

(6) Hulteen, J. C.; Martin, C. R. A General Template-Based Method for The Preparation of Nanomaterials. *J. Mater. Chem.* **1997**, *7*, 1075−1087.

(7) Wang, X.; Xu, S. Q.; Zhou, S. W.; Xu, W.; Leary, M.; Choong, P.; Qian, M.; Brandt, M.; Xie, Y. M. Topological Design and Additive Manufacturing of Porous Metals for Bone Scaffolds and Orthopaedic Implants: A Review. *Biomaterials* **2016**, *83*, 127−141.

(8) Wauthle, R.; van der Stok, J.; Yavari, S. A.; Van Humbeeck, J.; Kruth, J. P.; Zadpoor, A. A.; Weinans, H.; Mulier, M.; Schrooten, J. Additively Manufactured Porous Tantalum Implants. *Acta Biomater.* **2015**, *14*, 217−225.

(9) Velev, O. D.; Kaler, E. W. Structured Porous Materials via Colloidal Crystal Templating: From Inorganic Oxides to Metals. *Adv. Mater.* **2000**, *12*, 531−534.

(10) McCue, I.; Benn, E.; Gaskey, B.; Erlebacher, J. Dealloying and Dealloyed Materials. *Annu. Rev. Mater. Res.* **2016**, *46*, 263−286.

(11) Wittstock, A.; Zielasek, V.; Biener, J.; Friend, C. M.; Baumer, M. Nanoporous Gold Catalysts for Selective Gas-Phase Oxidative Coupling of Methanol at Low Temperature. *Science* **2010**, *327*, 319−322.

(12) Xu, C.; Xu, X.; Su, J.; Ding, Y. Research on Unsupported Nanoporous Gold Catalyst for CO Oxidation. *J. Catal.* **2007**, *252*, 243−248.

(13) Zeis, R.; Mathur, A.; Fritz, G.; Lee, J.; Erlebacher, J. Platinum-Plated Nanoporous Gold: An Efficient, Low Pt Loading Electrocatalyst for PEM Fuel Cells. *J. Power Sources* **2007**, *165*, 65−72.

(14) Friend, C. M.; Xu, B. J. Heterogeneous Catalysis: A Central Science for a Sustainable Future. *Acc. Chem. Res.* **2017**, *50*, 517−521.

(15) Zugic, B.; Wang, L. C.; Heine, C.; Zakharov, D. N.; Lechner, B. A. J.; Stach, E. A.; Biener, J.; Salmeron, M.; Madix, R. J.; Friend, C. M. Dynamic Restructuring Drives Catalytic Activity on Nanoporous Gold-Silver Alloy Catalysts. *Nat. Mater.* **2017**, *16*, 558−564.

(16) Snyder, J.; Fujita, T.; Chen, M. W.; Erlebacher, J. Oxygen Reduction in Nanoporous Metal-Ionic Liquid Composite Electrocatalysts. *Nat. Mater.* **2010**, *9*, 904−907.

(17) Bringa, E. M.; Monk, J. D.; Caro, A.; Misra, A.; Zepeda-Ruiz, L.; Duchaineau, M.; Abraham, F.; Nastasi, M.; Picraux, S. T.; Wang, Y. Q.; Farkas, D. Are Nanoporous Materials Radiation Resistant? *Nano Lett.* **2012**, *12*, 3351−3355.

DOI: 10.1021/acsami.7b04659
ACS Appl. Mater. Interfaces 2017, 9, 34172−34184

(18) Okulov, I. V.; Weissmuller, J.; Markmann, J. Dealloying-Based Interpenetrating-Phase Nanocomposites Matching the Elastic Behavior of Human Bone. *Sci. Rep.* **2017**, *7*, No. 20.
(19) Ding, D. Y.; Chen, Z. A pyrolytic, Carbon-Stabilized, Nanoporous Pd Film for Wide-Range H-2 Sensing. *Adv. Mater.* **2007**, *19*, 1996−1999.
(20) Biener, J.; Wittstock, A.; Zepeda-Ruiz, L. A.; Biener, M. M.; Zielasek, V.; Kramer, D.; Viswanath, R. N.; Weissmuller, J.; Baumer, M.; Hamza, A. V. Surface-Chemistry-Driven Actuation in Nanoporous Gold. *Nat. Mater.* **2009**, *8*, 47−51.
(21) Wada, T.; Ichitsubo, T.; Yubuta, K.; Segawa, H.; Yoshida, H.; Kato, H. Bulk-Nanoporous-Silicon Negative Electrode with Extremely High Cyclability for Lithium-Ion Batteries Prepared Using a Top-Down Process. *Nano Lett.* **2014**, *14*, 4505−4510.
(22) Lang, X.; Hirata, A.; Fujita, T.; Chen, M. W. Nanoporous Metal/Oxide Hybrid Electrodes for Electrochemical Supercapacitors. *Nat. Nanotechnol.* **2011**, *6*, 232−236.
(23) Harrison, J. D.; Wagner, C. The Attack of Solid Alloys by Liquid Metals and Salt Melts. *Acta Metall.* **1959**, *7*, 722−735.
(24) Wada, T.; Setyawan, A. D.; Yubuta, K.; Kato, H. Nano- to Submicro-Porous Beta-Ti Alloy Prepared from Dealloying in a Metallic Melt. *Scr. Mater.* **2011**, *65*, 532−535.
(25) McCue, I.; Ryan, S.; Hemker, K.; Xu, X. D.; Li, N.; Chen, M. W.; Erlebacher, J. Size Effects in the Mechanical Properties of Bulk Bicontinuous Ta/Cu Nanocomposites Made by Liquid Metal Dealloying. *Adv. Eng. Mater.* **2016**, *18*, 46−50.
(26) Tsuda, M.; Wada, T.; Kato, H. Kinetics of Formation and Coarsening of Nanoporous Alpha-titanium Dealloyed with Mg Melt. *J. Appl. Phys.* **2013**, *114*, No. 113503.
(27) Wada, T.; Kato, H. Three-Dimensional Open-Cell Macroporous Iron, Chromium and Ferritic Stainless Steel. *Scr. Mater.* **2013**, *68*, 723−726.
(28) Wada, T.; Yubuta, K.; Inoue, A.; Kato, H. Dealloying by Metallic Melt. *Mater. Lett.* **2011**, *65*, 1076−1078.
(29) Dicks, A. L. The Role of Carbon in Fuel Cells. *J. Power Sources* **2006**, *156*, 128−141.
(30) Cindrella, L.; Kannan, A. M.; Lin, J. F.; Saminathan, K.; Ho, Y.; Lin, C. W.; Wertz, J. Gas Diffusion Layer for Proton Exchange Membrane Fuel Cells - A Review. *J. Power Sources* **2009**, *194*, 146−160.
(31) Choi, H.; Kim, O. H.; Kim, M.; Choe, H.; Cho, Y. H.; Sung, Y. E. Next-Generation Polymer-Electrolyte-Membrane Fuel Cells Using Titanium Foam as Gas Diffusion Layer. *ACS Appl. Mater. Interfaces* **2014**, *6*, 7665−7671.
(32) Zhang, F. Y.; Advani, S. G.; Prasad, A. K. Performance of A Metallic Gas Diffusion Layer for PEM Fuel Cells. *J. Power Sources* **2008**, *176*, 293−298.
(33) McCue, I.; Gaskey, B.; Geslin, P. A.; Karma, A.; Erlebacher, J. Kinetics and Morphological Evolution of Liquid Metal Dealloying. *Acta Mater.* **2016**, *115*, 10−23.
(34) Geslin, P. A.; McCue, I.; Gaskey, B.; Erlebacher, J.; Karma, A. Topology-Generating Interfacial Pattern Formation during Liquid Metal Dealloying. *Nat. Commun.* **2015**, *6*, No. 8887.
(35) Chen-Wiegart, Y. C. K.; Wang, S.; McNulty, I.; Dunand, D. C. Effect of Ag−Au Composition and Acid Concentration on Dealloying Front Velocity and Cracking during Nanoporous Gold Formation. *Acta Mater.* **2013**, *61*, 5561−5570.
(36) Fujita, T.; Qian, L. H.; Inoke, K.; Erlebacher, J.; Chen, M. W. Three-dimensional Morphology of Nanoporous Gold. *Appl. Phys. Lett.* **2008**, *92*, No. 251902.
(37) Rosner, H.; Parida, S.; Kramer, D.; Volkert, C. A.; Weissmuller, J. Reconstructing a Nanoporous Metal in Three Dimensions: An Electron Tomography Study of Dealloyed Gold Leaf. *Adv. Eng. Mater.* **2007**, *9*, 535−541.
(38) Hu, K. X.; Ziehmer, M.; Wang, K.; Lilleodden, E. T. Nanoporous Gold: 3D Structural Analyses of Representative Volumes and their Implications on Scaling Relations of Mechanical Behaviour. *Philos. Mag.* **2016**, *96*, 3322−3335.
(39) Chen-Wiegart, Y.-c. K.; Wang, S.; Chu, Y. S.; Liu, W. J.; McNulty, I.; Voorhees, P. W.; Dunand, D. C. Structural Evolution of Nanoporous Gold during Thermal Coarsening. *Acta Mater.* **2012**, *60*, 4972−4981.
(40) Krekeler, T.; Straßer, A. V.; Graf, M.; Wang, K.; Hartig, C.; Ritter, M.; Weissmüller, J. Silver-Rich Clusters in Nanoporous Gold. *Mater. Res. Lett.* **2017**, *5*, 314−321.
(41) Pfeiffer, B.; Erichsen, T.; Epler, E.; Volkert, C. A.; Trompenaars, P.; Nowak, C. Characterization of Nanoporous Materials with Atom Probe Tomography. *Microsc. Microanal.* **2015**, *21*, 557−563.
(42) Wada, T.; Yubuta, K.; Kato, H. Evolution of A Bicontinuous Nanostructure via A Solid-State Interfacial Dealloying Reaction. *Scr. Mater.* **2016**, *118*, 33−36.
(43) De Andrade, V.; Deriy, A.; Wojcik, M. J.; Gürsoy, D.; Shu, D.; Fezzaa, K.; De Carlo, F. Nanoscale 3D Imaging at the Advanced Photon Source. *SPIE Newsroom* **2016**, 2−4.
(44) Jefimovs, K.; Vila-Comamala, J.; Stampanoni, M.; Kaulich, B.; David, C. Beam-Shaping Condenser Lenses for Full-Field Transmission X-ray Microscopy. *J. Synchrotron Radiat.* **2008**, *15*, 106−108.
(45) Chen-Wiegart, Y.-c. K.; Williams, G.; Zhao, C. H.; Jiang, H.; Li, L.; Demkowicz, M.; Seita, M.; Short, M.; Ferry, S.; Wada, T.; Kato, H.; Chou, K. W.; Petrash, S.; Catalano, J.; Yao, Y.; Murphy, A.; Zumbulyadis, N.; Centeno, S. A.; Dybowski, C.; Thieme, J. In *Early Science Commissioning Results of the Sub-micron Resolution X-ray Spectroscopy Beamline (SRX) in the Field of Materials Science and Engineering*, 23rd International Congress on X-ray Optics and Microanalysis, [Proc.]; Brookhaven National Laboratory: NY, Sept 14−18, 2015.
(46) Chen-Wiegart, Y.-c. K.; Camino, F. E.; Wang, J. Sample Preparation of Energy Materials for X-ray Nanotomography with Micromanipulation. *Chemphyschem* **2014**, *15*, 1587−1591.
(47) Gürsoy, D.; De Carlo, F.; Xiao, X.; Jacobsen, C. TomoPy: A Framework for the Analysis of Synchrotron Tomographic Data. *J. Synchrotron Radiat.* **2014**, *21*, 1188−1193.
(48) De Carlo, F.; Gursoy, D.; Marone, F.; Rivers, M.; Parkinson, Y. D.; Khan, F.; Schwarz, N.; Vine, D. J.; Vogt, S.; Gleber, S. C.; Narayanan, S.; Newville, M.; Lanzirotti, T.; Sun, Y.; Hong, Y. P.; Jacobsen, C. Scientific data exchange: a schema for hdf5-based storage of raw and analyzed data. Journal of Synchrotron Radiation. *J. Synchrotron Radiat.* **2014**, *21*, 1224−1230.
(49) Pelt, D. M.; De Andrade, V. Improved tomographic reconstruction of large-scale real-world data by filter optimization. *Adv. Struct. Chem. Imaging* **2017**, *2*, 17.
(50) Pelt, D.; Gürsoy, D.; Palenstijn, W. J.; Sijbers, J.; De Carlo, F.; Batenburg, K. J. Integration of tomopy and the astra toolbox for advanced processing and reconstruction of tomographic synchrotron data. *J. Synchrotron Radiat.* **2016**, *23*, 842−849.
(51) Miqueles, E. X.; Rinkel, J.; O'Dowd, F.; Bermúdez, J. S. V. Generalized titarenko's algorithm for ring artefacts reduction. *J. Synchrotron Radiat.* **2014**, *21*, 1333−1346.
(52) Pelt, D. M.; Batenburg, K. J. Accurately approximating algebraic tomographic reconstruction by filtered backprojection. In *Proceedings of the 2015 International Meeting on Fully Three-Dimensional Image Reconstruction in Radiology and Nuclear Medicine*, 2015.
(53) Schneider, C. A.; Rasband, W. S.; Eliceiri, K. W. NIH Image to ImageJ: 25 Years of Image Analysis. *Nat. Methods* **2012**, *9*, 671−675.
(54) Münch, B.; Holzer, L. Contradicting Geometrical Concepts in Pore Size Analysis Attained with Electron Microscopy and Mercury Intrusion. *J. Am. Ceram. Soc.* **2008**, *91*, 4059−4067.
(55) Chen-Wiegart, Y.-c. K.; DeMike, R.; Erdonmez, C.; Thornton, K.; Barnett, A.; Wang, J. Tortuosity Characterization of 3D Microstructure at Nano-Scale for Energy Storage and Conversion Materials. *J. Power Sources* **2014**, *249*, 349−356.
(56) Chen-Wiegart, Y.-c. K.; Wada, T.; Butakov, N.; Xiao, X. H.; De Carlo, F.; Kato, H.; Wang, J.; Dunand, D. C.; Maire, E. 3D Morphological Evolution of Porous Titanium by X-ray Micro- and Nano-Tomography. *J. Mater. Res.* **2013**, *28*, 2444−2452.
(57) Alkemper, J.; Voorhees, P. W. Three-Dimensional Characterization of Dendritic Microstructures. *Acta Mater.* **2001**, *49*, 897−902.

DOI: 10.1021/acsami.7b04659
ACS Appl. Mater. Interfaces 2017, 9, 34172−34184

(58) Li, L. *PyXRF*; GitHub, 2015.
(59) Marquardt, D. W. An Algorithm for Least-Squares Estimation of Nonlinear Parameters. *J. Soc. Ind. Appl. Math.* **1963**, *11*, 431−441.
(60) Lawson, C. L.; Hanson, R. J. *Solving Least Squares Problems*; SIAM (Society for Industrial and Applied Mathematics), 1995.
(61) Webb, S. *SAMK (Sam's Microprobe Analysis Kit)*, version 1.40; Stanford Synchrotron Radiation Laboratory, 2016.
(62) Bae, C. J.; Erdonmez, C. K.; Halloran, J. W.; Chiang, Y. M. Design of Battery Electrodes with Dual-Scale Porosity to Minimize Tortuosity and Maximize Performance. *Adv. Mater.* **2013**, *25*, 1254−1258.
(63) Chen, Q.; Sieradzki, K. Mechanisms and Morphology Evolution in Dealloying. *J. Electrochem. Soc.* **2013**, *160*, C226−C231.
(64) Lin, B.; Kong, L. X.; Hodgson, P. D.; Dumee, L. F. Impact of the De-Alloying Kinetics and Alloy Microstructure on the Final Morphology of De-Alloyed Meso-Porous Metal Films. *Nanomaterials* **2014**, *4*, 856−878.
(65) Lin, B.; Kong, L. X.; Hodgson, P. D.; Mudie, S.; Hawley, A.; Dumee, L. F. Controlled Porosity and Pore Size of Nano-Porous Gold by Thermally Assisted Chemical Dealloying - A SAXS Study. *RSC Adv.* **2017**, *7*, 10821−10830.
(66) Erlebacher, J. Mechanism of Coarsening and Bubble Formation in High-Genus Nanoporous Metals. *Phys. Rev. Lett.* **2011**, *106*, No. 225504.
(67) Kolluri, K.; Demkowicz, M. J. Coarsening by Network Restructuring in Model Nanoporous Gold. *Acta Mater.* **2011**, *59*, 7645−7653.
(68) Hingerl, F. F.; Yang, F. F.; Pini, R.; Xiao, X. H.; Toney, M. F.; Liu, Y. J.; Benson, S. M. Characterization of Heterogeneity in the Heletz Sandstone from Core to Pore Scale and Quantification of Its Impact on Multi-Phase Flow. *Int. J. Greenhouse Gas Control* **2016**, *48*, 69−83.
(69) Bruggeman, D. A. G. Berechnung Verschiedener Physikalischer Konstanten Von Heterogenen Substanzen. I. Dielektrizitätskonstanten und Leitfähigkeiten der Mischkörper aus Isotropen Substanzen. *Ann. Phys.* **1935**, *416*, 636−664.
(70) Thorat, I. V.; Stephenson, D. E.; Zacharias, N. A.; Zaghib, K.; Harb, J. N.; Wheeler, D. R. Quantifying Tortuosity in Porous Li-Ion Battery Materials. *J. Power Sources* **2009**, *188*, 592−600.
(71) Weissberg, H. L. Effective Diffusion Coefficient in Porous Media. *J. Appl. Phys.* **1963**, *34*, No. 2636.
(72) Kong, W.; Zhang, Q.; Xu, X. W.; Chen, D. F. A Simple Expression for the Tortuosity of Gas Transport Paths in Solid Oxide Fuel Cells' Porous Electrodes. *Energies* **2015**, *8*, 13953−13959.
(73) Xue, Y.; Markmann, J.; Duan, H. L.; Weissmuller, J.; Huber, P. Switchable Imbibition in Nanoporous Gold. *Nat. Commun.* **2014**, *5*, No. 4237.
(74) Kammer, D.; Voorhees, P. W. The Morphological Evolution of Dendritic Microstructures during Coarsening. *Acta Mater.* **2006**, *54*, 1549−1558.
(75) Chen, Y.-c. K.; Chu, Y. S.; Yi, J.; McNulty, I.; Shen, Q.; Voorhees, P. W.; Dunand, D. C. Morphological and Topological Analysis of Coarsened Nanoporous Gold by X-ray Nanotomography. *Appl. Phys. Lett.* **2010**, *96*, No. 043122.

DOI: 10.1021/acsami.7b04659
ACS Appl. Mater. Interfaces 2017, 9, 34172−34184